Cell Rearrangement Progression Along the Apical-Basal Axis is Linked with 3D Epithelial Tissue Structure

Erika M. Kusaka,* Sassan Ostvar,* Xiaoyun Liu, Xun Wang, Tianyi Liu, and Karen E. Kasza†
Department of Mechanical Engineering, Columbia University, New York, New York 10027, USA

(Received 24 July 2024; accepted 25 September 2025; published 12 January 2026)

Epithelial tissues undergo extensive structural remodeling during embryonic development. Tissue remodeling is often enabled by oriented cell rearrangements that are linked with patterns of mechanical stresses in the tissue and with tissue mechanical properties. Cell rearrangements and their links to tissue structure have largely been studied at the apical side of tissues at the level of adherens junctions. Less is known about the involvement of basolateral domains in cell rearrangements. Here we use live confocal imaging to quantify cell rearrangements, cell packing structure, and cell morphology in three dimensions in the converging and extending *Drosophila* germband epithelium. We report gradients in cell shapes and tissue structure along the apical-basal axis of the germband, suggesting that the apical and basolateral domains display distinct behaviors. Cell rearrangements initiate at apical as well as basolateral positions, with initiation frequencies also displaying a gradient along the apical-basal axis. Analyses of cell contact angles and nonmuscle myosin II localization patterns during cell rearrangements indicate that rearrangements can be actively driven in lateral as well as in apical regions of the tissue. Following initiation, rearrangements propagate across the apical-basal axis and lateral cell contacts remodel; these events involve scutoids and other complex 3D cell shapes as intermediate states. These findings uncover novel aspects of the cell rearrangements that drive dynamic remodeling of epithelia and reveal links between rearrangements and gradients in tissue structure along the apical-basal axis.

DOI: 10.1103/l5r5-pb9t

I. INTRODUCTION

Epithelial tissue sheets dynamically remodel and flow during development and in response to injury [1,2]. A primary mechanism driving epithelial remodeling in many contexts is local cell rearrangements that allow remodeling of cell-cell contacts without opening gaps in the tissue [3–6]. Significant research has focused on the proteins organizing junctional remodeling during cell rearrangements at the apical side of tissues [5–13], and how apical cell packing structure influences the solid-fluid tissue mechanical properties that resist tissue flow [14–21]. Less attention has been focused on the involvement of basolateral domains in cell rearrangements, although there is increasing evidence that basal protrusive activity contributes to cell rearrangements in many contexts in both epithelial and mesenchymal tissues [3,22–26]. It remains poorly understood how epithelial cell rearrangements occur along the full apical-basal axis in the 3D context of epithelia. Coupling between apical and basal sides of the tissue during cell rearrangements may be especially crucial in tall epithelia in which the apical and basal sides of the tissue are physically distant.

Recent studies have revealed that complex 3D cell shapes can naturally arise in some epithelial tissues [26–32]. In static epithelial tissue sheets that are curved or tilted, some columnar epithelial cells no longer take on the shapes of simple frusta and instead have different lateral cell neighbor contacts along the apical-basal axis in order to accommodate overall tissue shape [27–31]. These configurations are thought to be stable and result in cells "exchanging" neighbors along the apical-basal axis in a static tissue, and so have been referred to as "apical-basal cell rearrangements." These structures are associated with complex cell geometries known as *scutoids* [27,29,33]. In addition, transient apical-basal rearrangements and scutoids have recently been reported in proliferating epithelia in which new cells are generated and must be accommodated [32]. However, it is not known what 3D cell geometries might be involved in dynamic cell rearrangements in remodeling or flowing tissues, even in the context of relatively flat, nonproliferating tissue sheets.

Here we combine live confocal imaging, quantitative image analysis, and 3D reconstructions of remodeling cell-cell contacts to study how tissue structure varies and cell rearrangements proceed along the apical-basal axis over time in the converging and extending *Drosophila* germband epithelium. First, we show that cell shapes and tissue structure vary along the apical-basal axis of the tissue, suggesting varying behavior along this tissue axis. Next, we find that cell rearrangements can initiate at any depth along the apical-basal axis, although initiation is most frequent near the apical side of the tissue; rearrangements then propagate across the entire apical-basal axis of the tissue to produce complete cell

*These authors contributed equally to this work.
†Contact author: karen.kasza@columbia.edu

neighbor exchanges. Notably, the apical-basal gradient in cell rearrangement initiation frequencies mirrors the gradient in tissue structure along this axis, with cell rearrangements initiating most frequently in regions with high cell shape indices. Analyses of cell contact angles and nonmuscle myosin II (myosin) localization patterns indicate that rearrangement initiation and propagation can be actively driven all along the apical-basal axis. We explore the 3D geometries of cells that participate in dynamic cell rearrangements in the germband and find that scutoids and other complex geometries represent transient intermediate states in rearrangements, revealing novel features of cell rearrangements that mediate epithelial tissue shape changes. Finally, we investigate lateral cell-cell contact dynamics, uncovering the cell dynamics below the apical surface of the germband during convergent extension.

II. RESULTS

A. Cell shapes and tissue structure vary along the apical-basal axis of the *Drosophila* germband epithelium

We began by exploring how tissue structure varies along the apical-basal axis of the *Drosophila* germband epithelium. The germband converges and extends to elongate the head-to-tail body axis of the embryo in a process known as germband extension (GBE) [Fig. 1(a)] [7]. This rapid tissue flow is mediated by oriented cell rearrangements that are thought to be driven by planar polarized patterns of actomyosin contractility at adherens junctions near the apical side of the tissue [8–10], although activities at the basal side have also been reported [23]. Recently, our group and others showed that the onset of cell rearrangements can be predicted by cell shapes at apical cross sections of the tissue, which can be understood as a transition from solid-like to more fluid-like tissue behavior [15,16,21,34,35]. However, it is not known whether cell shapes vary along the apical-basal axis of the ≈30 μm tall columnar germband epithelium or how any variations might be linked with tissue remodeling.

We acquired confocal timelapse movies of the germband of wild-type embryos expressing a cell membrane marker with z slices taken at 1 μm intervals and spanning the entire tissue [Fig. 1(a)]. We segmented the images at z slices with sufficient image quality (typically z = 2–21 μm) [Fig. 1(b)] and quantified cross-sectional cell shapes in each z slice using the average cell shape index, $\bar{p}^{2D}$, which characterizes whether cells have long or short contacts with their neighbors in the 2D cross section [Fig. 1(b)] [14,15,17,36]. Consistent with prior reports, $\bar{p}^{2D}$ increases over time at the apical side of the tissue [Figs. 1(c), 1(e), 1(f)] [21]. This is accompanied by an increase in vertex coordination number, $\mathcal{Z}$, over time [Fig. 1(e″)], which reflects an increase in high-order vertices that form transiently as intermediates during cell rearrangements as the tissue remodels. The increase in $\bar{p}^{2D}$ over time is observed in all z slices, but we also find that $\bar{p}^{2D}$ varies along the apical-basal axis [Figs. 1(c), 1(e), 1(f); Supplemental Material Fig. S1 [37]]. $\bar{p}^{2D}$ is highest at the apical side of the tissue and then decreases in a gradient towards the basal side [Fig. 1(f)]. The gradient arises from $\bar{p}^{2D}$ increasing earlier at apical compared to basolateral positions around the onset of GBE (T = 0 min) [Figs. 1(e), 1(f)]. The gradient becomes less pronounced by around T = 10 min as $\bar{p}^{2D}$ increases at more basolateral positions [Fig. 1(f)].

Because the apical side of the germband is anisotropic in the plane of the tissue [21], we also quantified anisotropy using the cell shape alignment index, Q, derived from a triangulation of cell centroids [Figs. 1(b), 1(d)] [38]. Consistent with prior work, at the apical side of the tissue there is a peak in Q around T = 0 [Figs. 1(e′), 1(g)], due to stretching of the germband by the invaginating ventral furrow [21,39,40]. We again find that alignment is highest at the most apical z slices [Figs. 1(d), 1(e′), 1(g); Supplemental Material Fig. S1 [37]] suggesting that the stretch from ventral furrow invagination most strongly affects the apical side of the tissue. Therefore, similar to $\bar{p}^{2D}$, Q exhibits an apical-basal gradient.

We wondered how the observed apical-basal gradients in planar cell packing structure relate to epithelial cell organization. To estimate a characteristic length scale for the apical-basal gradients, we calculated the tissue depth at which $\bar{p}^{2D}$ and Q reached half their maximum apical values. We found the characteristic length scale is ∼6 μm for $\bar{p}^{2D}$ and ∼8 μm for Q for the analyzed tissue depths [Figs. 1(f′), 1(g′)]. Both vary weakly over time with some embryo-to-embryo variability [Figs. 1(f′), 1(g′)]. These length scales correspond to tissue depths just below the level of apical adherens junctions. The appearance of the apical-basal gradients in cell packing structure correlates with the onset of anisotropic actomyosin-generated stresses at adherens junctions [8,9,11,41–43], suggesting that these gradients may arise from propagation of apical stress patterns along the apical-basal axis.

Taken together, these results demonstrate that there are structural gradients along the apical-basal axis of the germband that evolve over time during convergent extension, suggesting varying environments along this axis that could potentially be linked to the progression of cell-cell contact remodeling during cell rearrangements.

B. Cell rearrangements initiate at various tissue depths and then propagate across the entire apical-basal axis of the tissue

We noticed in our structural measurements that $\bar{\mathcal{Z}}$ is somewhat higher at more apical z slices around the onset of GBE [Fig. 1(e″); Supplemental Material Fig. S1, Fig. S2 [37]]. Although this effect is subtle, it suggested that cell rearrangements might initiate at the apical side of the tissue, near actomyosin enrichment at adherens junctions, around the onset of GBE and then propagate across the tissue. To investigate this possibility, we first analyzed a set of manually identified cell rearrangements over time and along the apical-basal axis [Fig. 2(a)], focusing on four-cell rearrangements called T1 processes.

We identified the z position of each rearrangement initiation site where a high-order vertex, a four-cell vertex in this case, first forms via contraction of a cell-cell contact, and we found a gradient in initiation frequency along the apical-basal axis [Figs. 2(b), 2(c)]. Half of the rearrangements analyzed initiated within the most apical 4 μm, but we also found significant numbers of rearrangements initiating all along the apical-basal axis [Fig. 2(c)], similar to a recent study [26]. This was unexpected as we had anticipated

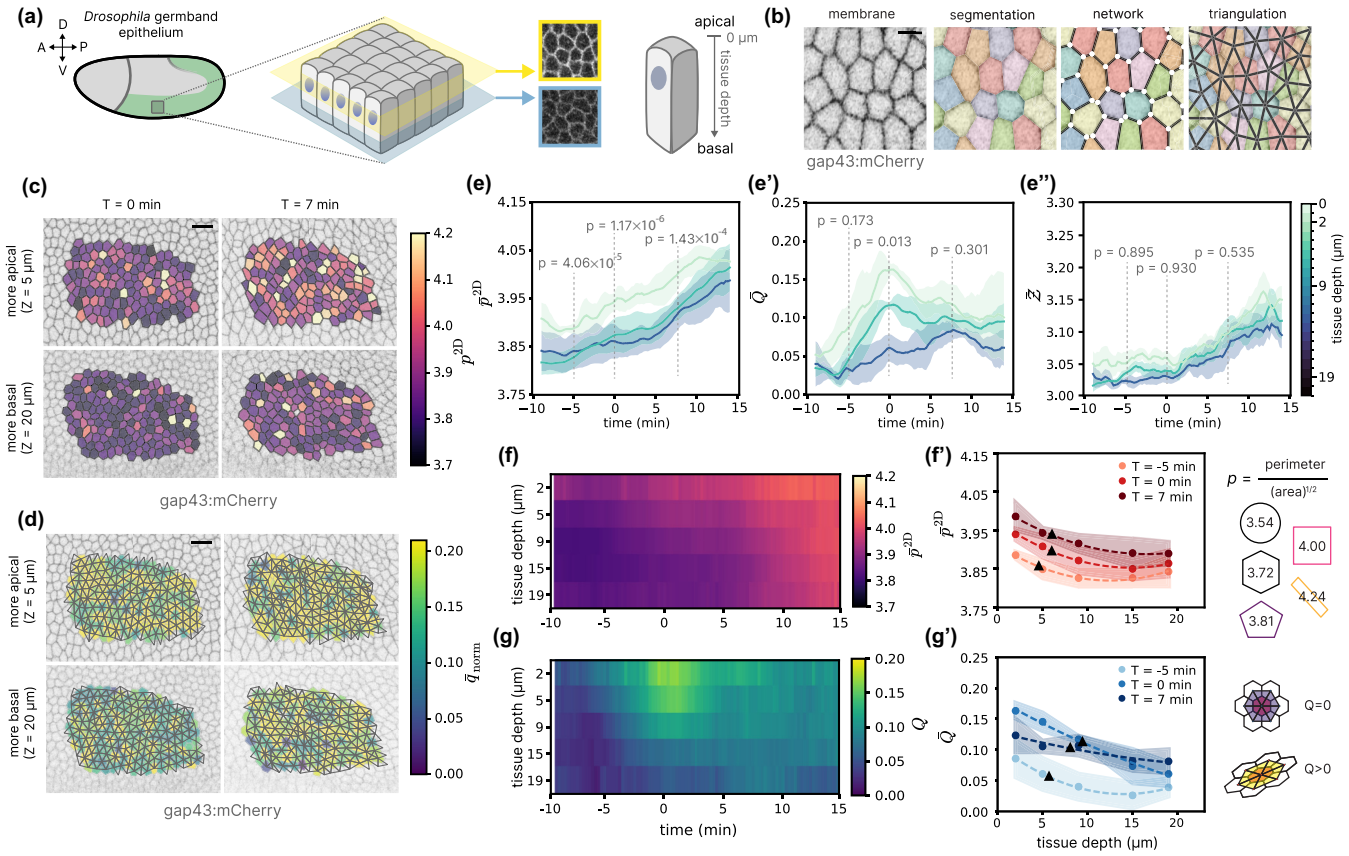

FIG. 1. Cell shapes and tissue structure vary along the apical-basal axis in the *Drosophila* germband epithelium. (a) Schematic of the *Drosophila* germband epithelium during germband extension (GBE) (left). Schematic of the germband epithelial tissue with example confocal images of cell shapes at apical and basolateral positions in the germband. Schematic of apical-basal axis mapped onto a cell with $z = 0$ set at the apical surface. (b) Cell membranes labeled with gap43:mCherry are visualized by confocal microscopy. At each z position along the apical-basal axis, cells are segmented and represented as straight edged polygons that tile the plane to quantify cell shapes and vertex coordination number. The polygon network is triangulated for quantification of cell shape alignment. Scale bar, 5 μm. (c) The cell shape index from confocal z slices, p^{2D}, for individual cells at apical (top) and basolateral (bottom) z positions in the tissue at the onset of GBE ($T = 0$ min, left) and 7 min after the onset of GBE (right). Scale bar, 15 μm. (d) Triangulation used to calculate the cell shape alignment index, Q. The color of each cell represents the local tissue alignment quantified by the average norm of the triangle nematic directors (q) for triangles that have a vertex at the cell centroid. Scale bar, 15 μm. (e) Time series of the average cell shape index, $\bar{p}^{2D}$, (e') the cell shape alignment index, Q, and (e″) the vertex coordination number, $\mathcal{Z}$, at three z positions along the apical-basal axis of the tissue. For (e), (e′), and (e″), data are the average of $N = 3$ embryos, and shaded regions represent the standard deviation (SD) between embryos. P values at time points −5, 0, and 7 min (Kruskal-Wallis test). (f) Heat map of $\bar{p}^{2D}$ along the apical-basal axis over time. Data represent the average of $N = 3$ embryos. (f′) $\bar{p}^{2D}(z)$ at three time points. For each time point, the data are fit to a polynomial curve (dashed line) to determine the characteristic length scale at which $\bar{p}^{2D}(z)$ falls to half of its maximum value (black triangles). Data are the average of $N = 3$ embryos, and shaded regions represent the SD between embryos. Right: Schematic of the cell shape index with example shapes. (g) Heatmap of Q along the apical-basal axis over time. Data represent average of $N = 3$ embryos. (g′) Average Q along the apical-basal axis at three time points. For each time point, the data are fit to a polynomial curve to determine the characteristic length scales (black triangles). Data are the average of $N = 3$ embryos, and shaded regions represent the SD between embryos. Right: Schematic of Q with examples of low and high alignment.

that rearrangement initiation would be restricted to apical adherens junctions [9,10] or basal sites of protrusive activity [23]. However, this is consistent with a recent observation of myosin localization at rearranging cell contacts all along the apical-basal axis [26]. Lateral rearrangement initiation has also recently been observed in the neighboring presumptive mesoderm tissue but is specifically associated with the presence of a second, more lateral tier of adherens junctions in those cells [44]. In addition, we identified a subset of multifocal rearrangements with nearly simultaneous initiation at both apical and more basolateral z positions [Fig. 2(b)]. We categorized rearrangements into four groups based on their initiation type [Fig. 2(b)]. Initiation in the top 0–5 μm around the level of adherens junctions (apical) was most prevalent at 60% ± 19%. Initiation in the next 10 μm (lateral) was next most prevalent at 27% ± 17%. Initiation at z positions below 15 μm (basolateral) or at multiple sites (multifocal) were relatively rare at 6% ± 7% and 7% ± 6%, respectively [Fig. 2(d); Supplemental Material Fig. S2B [37]]. Notably, the cell rearrangement initiation frequency increased strongly with the value of $\bar{p}^{2D}$ along the apical-basal axis [Fig. 2(c), inset]. These results demonstrate that cell rearrangements initiate in a

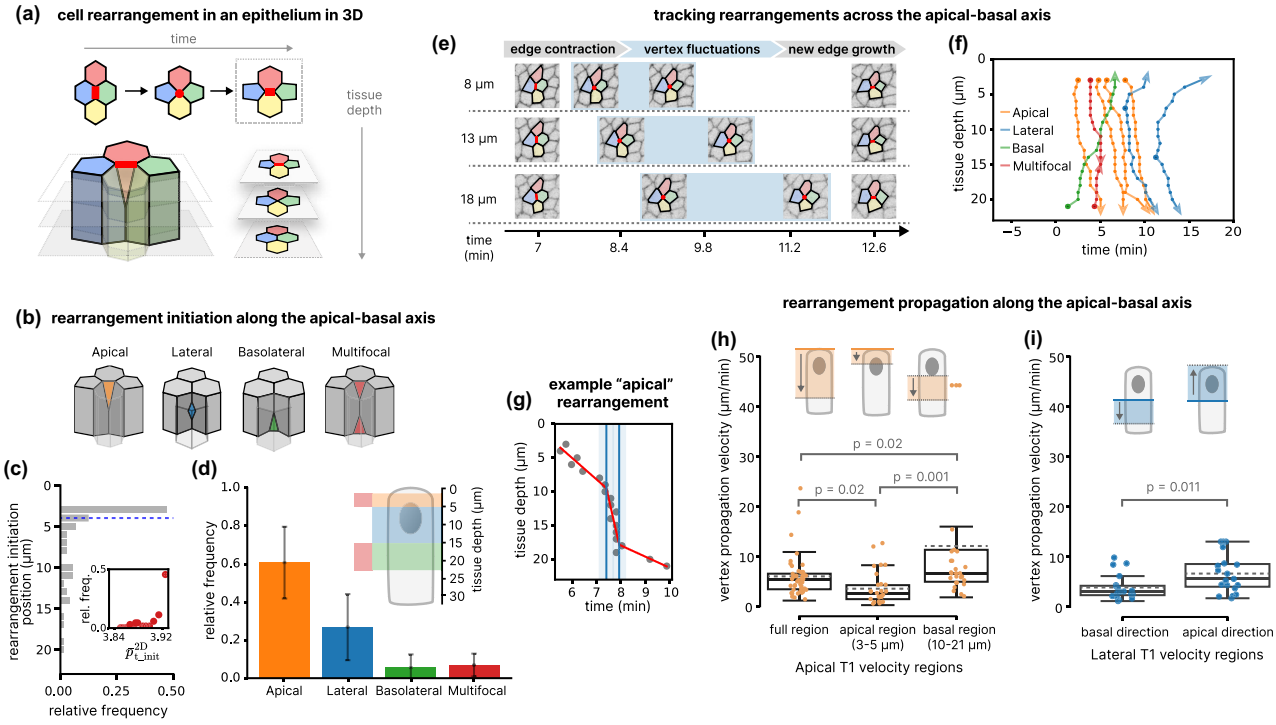

FIG. 2. Cell rearrangements initiate at various tissue depths and then propagate along the apical-basal axis. (a) Schematic of a cell rearrangement involving four cells (T1 process) that initiates at the apical side of the tissue, highlighting how cell contacts change in time and space. (b) Schematics of rearrangements that initiate at different positions along the apical-basal axis. (c) Histogram of rearrangement initiation locations along the apical-basal axis (T1 processes only). Position of half the cumulative sum of rearrangements is represented by the blue dashed line. Inset: Frequency of cell rearrangement initiation vs the average value of $\bar{p}^{2D}$ at the onset of GBE. $n = 73$ rearrangements were pooled from $N = 3$ embryos. (d) Frequency of each type of rearrangement. Mean and SD between $N = 3$ embryos. Inset: Rearrangement initiation was classified as apical for 0–5 µm, lateral for 5–15 µm, and basolateral for 15+ µm. Rearrangement initiation was classified as multifocal if there were both apical and basolateral sites of initiation. (e), (f) Manual tracking of cell rearrangement initiation and propagation along the apical-basal axis in confocal z stacks. (e) Example of a rearrangement that initiates at the apical side. Images highlighting the four cells in the rearrangement at three z positions and various time points. Vertices (red circles), changing cell contacts (red lines). Blue regions are time points over which the vertex fluctuates before resolving to form a new contact. (f) Example vertex trajectories along the apical-basal axis over time for different types of rearrangements. Vertex initiation points (circles) and direction of vertex propagation (arrow heads) are indicated. (g) Example of a vertex trajectory with a piecewise linear regression analysis (red lines) used to calculate vertex propagation velocities. (h) Vertex propagation velocity magnitudes for apically initiated rearrangements. Velocity varies along the apical-basal axis. Median, solid line. Mean, dashed line. Friedman test, $p = 6.25\text{E-}7$; p values from a *post hoc* Nemenyi test shown on plot. Velocities separated by embryo are shown in Supplemental Material Fig. S3C [37]. (i) Vertex propagation velocity magnitudes for laterally initiated rearrangements. Velocities are separated into propagation in the apical and basal directions. Median, solid line; mean, dashed line. Wilcoxon signed-rank test, p value shown on plot.

gradient along the apical-basal axis that is reminiscent of the gradients observed in $\bar{p}^{2D}$ and Q, indicating a link between tissue structure variations and cell rearrangement initiation along the apical-basal axis.

Next, we examined how cell rearrangements proceed after initiation by manually tracking the propagation of high-order vertex formation along the apical-basal axis over time [Figs. 2(e), 2(f)]. For all rearrangement types, we found that once initiated, the high-order vertex propagates along the apical-basal axis [Fig. 2(f); Supplemental Material Fig. S2A [37]], similar to a recent observation [26]. Apical initiations propagate basally; basolateral initiations propagate apically; lateral initiations propagate both apically and basally; and multifocal initiations propagate laterally. We noticed that the velocity of vertex formation or "vertex velocity" seemed to vary as the vertex moved along the apical-basal axis [Figs. 2(f), 2(g)]. For roughly 70% of apically initiated rearrangements, vertex velocity was slower near the apical side of the tissue and increased as the vertex moved basally [Figs. 2(g), 2(h); Supplemental Material Fig. S3A [37]], similar to a previous observation [44]. The change in velocity often occurred at tissue depths between 5 and 10 µm [Supplemental Material Fig. S3B [37]], similar to the depths at which $\bar{p}^{2D}$ and Q decreased significantly [cf. Figs. 1(f′), 1(g′)]. In contrast, for laterally initiated rearrangements, vertex propagation towards the apical side was faster than towards the basal side [Fig. 2(i)]. Overall, we find that typical vertex propagation velocities are ≈5 µm/min. For comparison, this is faster than the ≈1 µm/min velocity of furrow ingression during the fast phase of cellularization that forms the germband epithelium [45,46] and slower than the ≈20 µm/min propagation speed of cell area oscillations in the germband [26].

Taken together, these results demonstrate that cell rearrangements initiate in a gradient along the apical-basal axis

and then propagate at speeds linked to tissue depth across the apical-basal axis. Notably, the gradient in initiation frequency mirrors the gradient in tissue structure along the apical-basal axis, suggesting a link between high $\bar{p}^{2D}$ and Q and high rearrangement initiation rates. Moreover, the observed changes in vertex propagation velocities along the apical-basal axis suggest that the local structural environment of the tissue is linked with local cell contact remodeling.

C. Protein localization patterns and cell-cell contact angles suggest that rearrangement initiation and propagation may be actively regulated

Many epithelial cell rearrangements are thought to be actively driven by contractile tensions generated by myosin and F-actin and coordinated with remodeling of E-cadherin-based cell-cell adhesions [1,5]. During *Drosophila* germband extension, studies of protein localization patterns associated with cell rearrangements have largely focused on the apical side of the tissue, at and above the level of adherens junctions, where myosin, F-actin, and E-cadherin are enriched in a planar polarized pattern thought to drive and orient rearrangements [5,8,9]. To characterize the apical-basal distribution of these proteins, we first quantified myosin, E-cadherin, and F-actin localization along lateral cell membranes in fixed embryos [Figs. 3(a)–3(b′)]. Both myosin and E-cadherin are distributed in gradients along the apical-basal axis, consistent with previous observations [8]. Fluorescence intensities are highest apically near adherens junctions and fall to half the maximum intensity values at depths of 3–5 μm [Figs. 3(b), 3(b′)], similar to the characteristic length scales of the gradients in $\bar{p}^{2D}$, Q, and rearrangement initiation [cf. Figs. 1(f′), 1(g′), and 2(c)]. In contrast, F-actin localizes at both apical and basolateral cell membranes, with a more pronounced accumulation near the basal tissue surface around the onset of germband extension [Figs. 3(b), 3(b′)]. These results indicate that gradients in tissue structure and rearrangement initiation may be linked with gradients in the contractile and adhesive machinery.

To more directly explore the links between protein localization and cell rearrangement dynamics, we next imaged fluorescently tagged myosin and cell membrane markers along the apical-basal axis during germband extension in live embryos. In addition to the apical enrichment of myosin at the level of adherens junctions, we observed transient myosin enrichment at some lateral cell-cell contacts that are shrinking during both T1 rearrangements involving four cells and rosette rearrangements involving five or more cells [Fig. 3(d), 3(d′), Supplemental Material Fig. S4 [37]], consistent with a recent study [26]. Around 33% (13/40) of all rearrangements analyzed showed some detectable lateral myosin enrichment. Among laterally initiated rearrangements, approximately 45% (9/20) exhibited lateral myosin enrichment, while the remainder showed no discernible lateral myosin signal [Fig. 3(c)]. Lateral myosin was also observed in some apically initiated rearrangements (∼15%, 2/13) as the rearrangement propagated basally [Fig. 3(c)]. Notably, all laterally initiated rearrangements with lateral myosin enrichment show apical propagation of the myosin intensity, which precedes the apical propagation of the high-order vertex [Fig. 3(i), Supplemental Material Fig. S3D [37]], suggesting that myosin plays an active role in driving rearrangement propagation in the lateral domain. In rearrangements lacking detectable myosin signal, we cannot rule out low levels of myosin at or below background fluorescence. Alternatively, this could point to either an alternative myosin-independent mechanism that can actively drive rearrangement or to some lateral rearrangement behaviors being passive responses to active forces originating elsewhere. Taken together, these patterns suggest that transient lateral myosin accumulation is associated with high-order vertex formation and cell rearrangement behavior in many rearrangements, supporting a role for active, myosin-generated tension at lateral contacts in tissue remodeling.

To help distinguish between a model in which cell rearrangement progression is actively driven by local forces distributed along lateral contacts and a model in which lateral rearrangement behavior is a passive relaxation in response to active force originating elsewhere in the tissue, e.g., near adherens junctions, we analyzed cell contact angles around contacts that shrink to initiate cell rearrangement [41,47–51]. Unlike prior work that focused on tissue depths near apical adherens junctions [41,49–51], here we analyzed cell contact angles in 2D slices at each tissue depth. The general approach of inferring tensions from cell contact angles assumes that tensions at cell contacts equilibrate rapidly enough that the tissue is close to mechanical equilibrium [47,48,50] and has been validated and used to infer tensions near adherens junctions in both static and dynamically remodeling tissues [47–50], including the *Drosophila* germband [49–51]. We used cell contact angles at each tissue depth as a readout for the local tension patterns at the shrinking edge relative to neighboring edges. Contact angles below 120° indicate higher tension in the shrinking edge, characteristic of an "active" rearrangement driven by local tension patterns, while angles close to 120° indicate equal tensions at cell edges, characteristic of a "passive" rearrangement driven by external forces, as recently described [51]. On average, we observe that contact angles become more acute during edge contraction just prior to vertex formation at each tissue depth [Figs. 3(e)–3(h)]. Notably, this is true both in the apical domain near adherens junctions and in the lateral domain, suggesting active tensions driving rearrangements all along the apical-basal axis [Figs. 3(f), 3(h)].

Comparing myosin localization and cell contact angles across different z positions, we see that rearrangements exhibit a larger decrease in contact angle when myosin accumulation is present at the tissue depth where the rearrangement initiates, such as in lateral rearrangements with lateral myosin and in apical rearrangements with apical myosin [Fig. 3(j)], suggesting that local myosin contractility actively drives contact angle changes during these rearrangements. In contrast, in laterally initiated rearrangements without detectable lateral myosin accumulation, we see smaller contact angle changes [Fig. 3(j)], suggesting that these rearrangement behaviors might be the result of passive relaxation in response to external forces.

Taken together, these findings demonstrate a role for active, myosin-dependent processes in the lateral domain during cell rearrangements and also suggest the possibility that a fraction of rearrangement behaviors may be passive responses to active forces generated in other regions of the tissue.

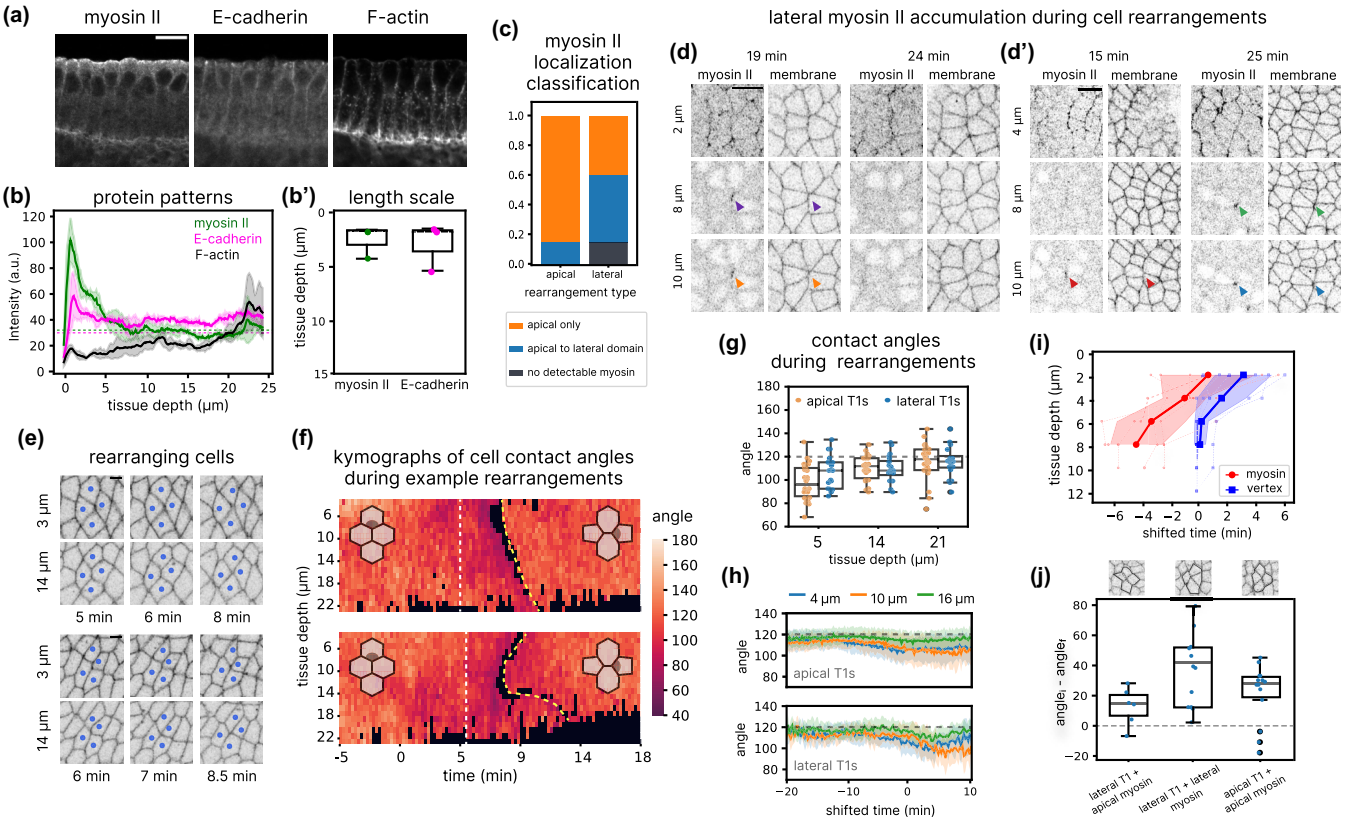

FIG. 3. Protein localization patterns and cell-cell contact angles along the apical-basal axis during cell rearrangement. (a) Confocal fluorescence images of nonmuscle myosin II, E-cadherin, and F-actin in germband epithelial cells in a representative fixed embryo at the onset of germband extension (stage 6). Apical up, anterior left. Scale bar, 10 μm. (b) Average intensity of myosin, E-cadherin, and F-actin, along the apical-basal axis of the embryo in shown in (a). The shaded regions represent the standard deviation (SD) between five sampled regions. Dashed lines indicate average cytoplasmic intensity for each channel, used in background subtraction in (b′). (b′) Tissue depths at which the intensity of myosin or E-cadherin reaches half the maximum values, based on intensity profiles as shown in (b). $N = 3$ embryos (stages 6 and 7). (c) Fraction of rearrangements with detectable myosin accumulation only in the apical domain (0–6 μm), in apical and lateral domains (0–15 μm), or with no detectable accumulation, in apically initiated ($n = 13$) and laterally initiated ($n = 20$) rearrangements identified in live confocal fluorescence movies. (d)–(d′) Example confocal images of fluorescently-tagged myosin and a membrane marker for a T1 rearrangement (d) and rosette rearrangement (d′). Arrowheads highlight myosin accumulation and the corresponding locations in the cell membrane channel. The onset of GBE is at $t = 0$ min. Scale bars, 10 μm. See extended set of images in Supplemental Material Fig. S4 [37]. (e) Example confocal fluorescence images of cell rearrangements used for cell contact angle analyses in panels (f)–(h) and (j). An apically initiated (top) and a laterally initiated (bottom) rearrangement at various z planes and time points. Scale bar, 5 μm. (f) Heat maps of cell contact angles (degrees) along the apical-basal axis and over time for the example apically initiated (top) and laterally initiated (bottom) rearrangements from (e). The white dashed line indicates the time of rearrangement initiation measured as the first formation of a high-order vertex anywhere along the apical-basal axis. The yellow dashed line indicates the time points associated with the formation of the new cell edge. Left and right schematics show the angles being measured before and after new edge formation. Black regions in the heat map represent frames when the angle cannot be determined. (g) Comparison of cell contact angles (degrees) at various z planes for apically and laterally initiated cell rearrangements at the time of rearrangement initiation measured as the first time point of high-order vertex formation. n(apical) $= 12$ and n(lateral) $= 10$ cell rearrangements. Median, solid line. (h) Average cell contact angle (degrees) over time at various z planes during apically (top) or laterally (bottom) initiated cell rearrangements, with time shifted by the rearrangement time [cf. definition in Figs. 5(a) and 5(b)]. Shaded regions represent the standard deviation between rearrangements. n(apical) $= 14$ and n(lateral) $= 10$ cell rearrangements. (i) Myosin and high-order vertex propagation over time and along the apical-basal axis for laterally initiating T1 rearrangements that display detectable lateral myosin accumulation ($n = 6$). Rearrangements are registered to the initial time point of high-order vertex formation ($t = 0$). Bold lines represent the average myosin and high-order vertex propagation trajectories. Shaded regions indicate the standard deviation between rearrangements. Data from individual rearrangements are represented by smaller markers and are shown separately in Supplemental Material Fig. S3D [37]. (j) Change in contact angle (degrees) over time preceding initiation of lateral and apical T1 rearrangements with distinct myosin localization patterns (see c). Initial angle is measured 5 min before high-order vertex formation, and final angle is measured immediately before vertex formation. Median is represented by the gray line. Data is from $n = 3$–9 rearrangements per group, with two angles measured for each rearrangement. Top: Representative confocal images for each category.

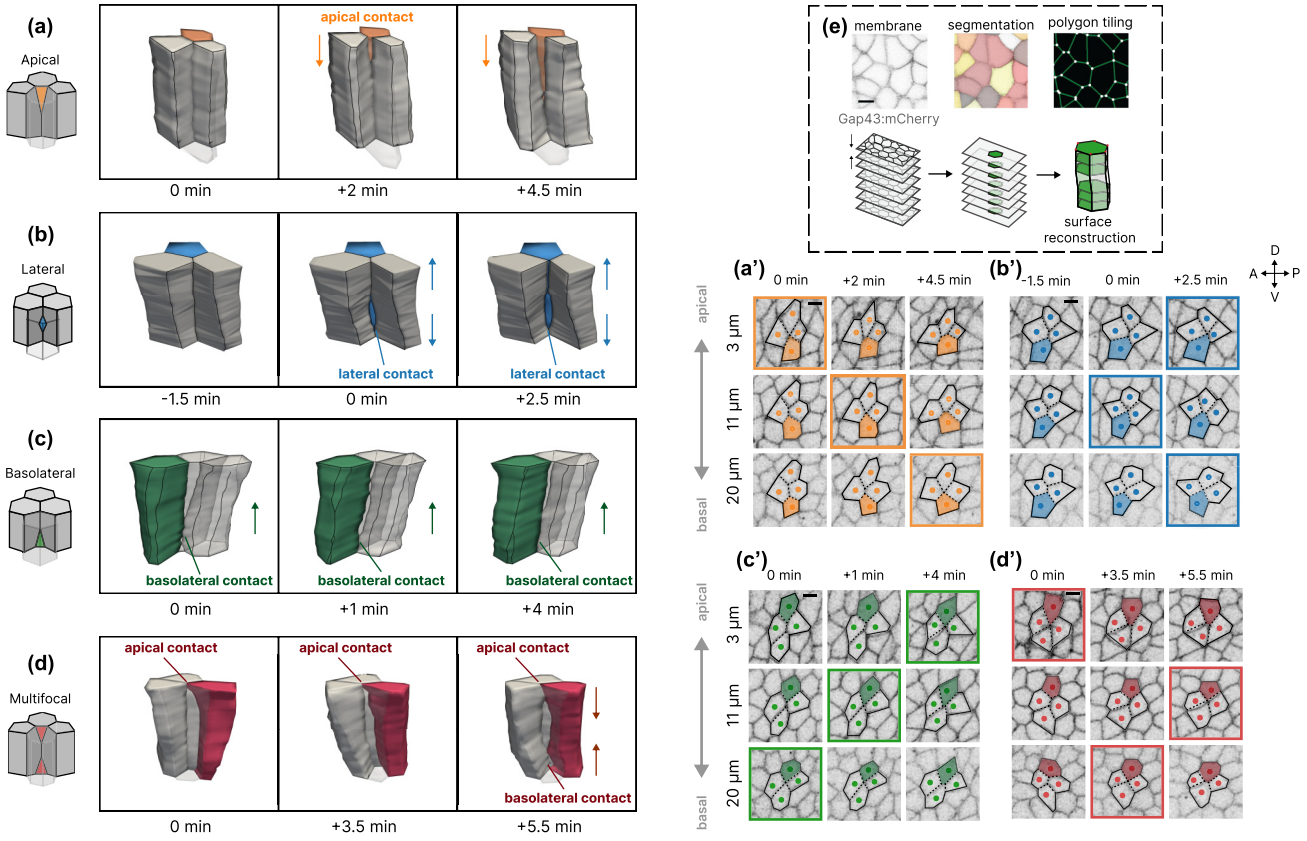

FIG. 4. Complex 3D cell geometries are intermediate states during dynamic cell rearrangements. 3D reconstructions of rearrangements with apical (a), lateral (b), basolateral (c), and multifocal (d) initiation, highlighting the variety of transitional cell geometries involved in dynamic cell rearrangements. Rearrangements with apical or basolateral initiation are associated with transient scutoids. Rearrangements with lateral or multifocal initiation are associated with more complex cell geometries and lateral cell-cell contacts. (a′)–(d′) Confocal fluorescence images of the example rearrangements from (a)–(d) at multiple z planes and time points. In each panel, cell edges and contacts are highlighted with solid lines and dotted lines respectively and frames with high-order vertices are boxed. Scale bars, 5 µm. (e) Methods for 3D reconstruction of cell shapes and lateral cell-cell contacts as triangulated surfaces based on confocal imaging data.

D. Complex 3D cell geometries are intermediate states during dynamic cell rearrangements

Our observations of high-order vertex formation followed by propagation along the apical-basal axis led us to investigate the 3D shapes of cells and their lateral cell contacts during cell rearrangements. We used single-cell tracking and a custom 3D reconstruction pipeline to represent the geometry of lateral cell-cell contacts as triangulated surfaces using information from 2D cell outline networks in each z plane [Figs. 4(a)–4(e); Materials and Methods].

We found a variety of complex 3D cell geometries that are transient intermediate states as cells change shape during rearrangements [Figs. 4(a)–4(d)]. These cell geometries correspond to distinct rearrangement initiation types: rearrangements initiated apically and basolaterally involve transient scutoids [Figs. 4(a), 4(a′), 4(c), 4(c′)], while rearrangements initiated laterally or multifocally involve more complex cell contact patterns [Figs. 4(b), 4(b′), 4(d), 4(d′)]. These transient, intermediate cell geometries are typically resolved as the new lateral cell-cell contact first expands along the apical-basal axis to form a tall and narrow facet that subsequently widens; cells eventually recover their geometries as pyramidal frusta [Figs. 4(a)–4(d)].

Scutoids were first identified as equilibrium cell shapes in curved epithelia [27,29,33] and have recently been reported as transient states following cell proliferation in the sea star embryo [32]. The transient scutoids we find here are distinct in that they occur in a nonproliferating epithelium in which cell numbers are not changing, so that the transient scutoids must be induced by other factors, such as dynamic actomyosin-generated stress patterns that vary along the apical-basal axis of the tissue [26]. In the germband, these stress patterns likely arise from the planar polarized myosin pattern at apical adherens junctions and transient myosin accumulations at lateral cell contacts, and are linked with the observed gradients in tissue structure along the apical-basal axis. The basolateral rearrangements we find here may be related to rearrangements initiated by basal protrusive activity in the germband [23], although we do not resolve the most basal side of the tissue in our analyses. To our knowledge, the transient cell geometries we observe during lateral and multifocal rearrangements represent new classes of epithelial cell geometries.

E. Lateral cell contact remodeling during cell rearrangement

Remodeling of lateral cell-cell contacts is the fundamental process mediating epithelial cell rearrangements, but the

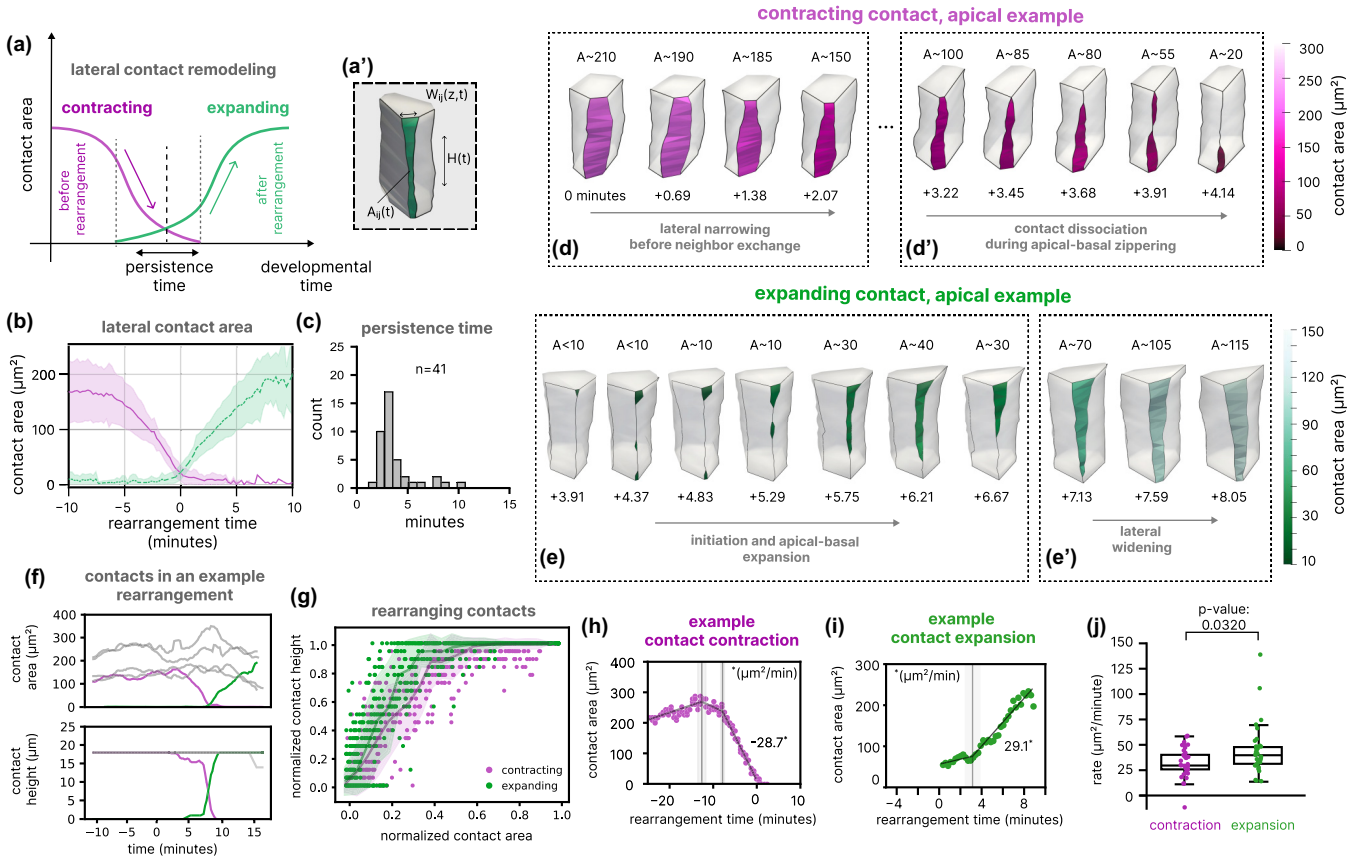

FIG. 5. Lateral cell contact remodeling during cell rearrangement. (a) Model of lateral cell contact remodeling during a cell rearrangement (T1 process), highlighting the time evolution of contracting and expanding lateral contacts; the persistence time is defined by the interval where both the contracting and expanding contacts are present (Materials and Methods). (a′) Schematic illustrating the apical-basal and lateral growth of a new contact. (b) Averaged time series of areas of contracting and expanding contacts during cell rearrangement, centered by the rearrangement time $t = 0$ for $n = 41$ rearrangements in $N = 2$ embryos. (c) Distribution of persistence times. (d), (d′) Sample timelapse of a contracting contact in an apically initiated rearrangement; highlighted are two distinct steps in the process: initial lateral narrowing of the contact (d) followed by disappearance of the narrow contact along the apical-basal axis (d′); color indicates the value of the contact surface area. See additional examples in Supplemental Material Fig. S5C [37]. (e), (e′) Sample timelapse of an expanding contact; highlighted are two distinct steps in the process: initial establishment of a narrow and tall contact (e) followed by widening of the contact (e′); color indicates the value of the contact surface area. See additional example in Supplemental Material Fig. S5D [37]. (f) Time series of areas (top) and heights (bottom) of lateral contacts in cells associated with an example T1 cell rearrangement. Contracting contacts are shown in purple, expanding contacts in green, and stable contacts in gray. (g) Height vs area for contracting and expanding lateral contacts from $n = 15$ cell rearrangements, values normalized to the respective maximum values for each contact. Solid lines represent average trajectories for contracting and expanding contacts. Shaded regions indicate the standard deviation between contacts. (h) Example contact area time series for a contracting contact. Slope in region of rapid area decrease is shown. (i) Example contact area time series for an expanding contact. Slope in region of rapid area increase is shown. (j) Rates of rapid contact contraction and expansion defined in (h) and (i). See extended analysis of lateral contact area changes in Supplemental Material Figs. S5–S7 [37].

nature of lateral contacts is poorly understood. This is due in large part to the challenge of quantitatively analyzing lateral cell surfaces compared to the more accessible apical or basal planar cross sections in which cell contacts appear as polygon edges. To explore the process of lateral cell contact remodeling, we leveraged our reconstructions of lateral cell contact surfaces to quantify how existing contacts contract and new contacts grow during cell rearrangements [Figs. 5(a), 5(a′); Supplemental Material Fig. S5A [37]].

For each cell rearrangement, we measured the areas of the contracting and expanding contacts and defined $t = 0$ min as the time point at which these curves cross [Figs. 5(a), 5(b)]. On average, full contact expansion or contraction each take ∼5–10 min, and these two processes display temporal overlap ($n = 41$ rearrangements in $N = 2$ embryos) [Fig. 5(b)]. We defined a persistence time for each rearrangement as the interval spanning the first appearance of the expanding contact and the last disappearance of the contracting contact [Fig. 5(a)]. Equivalently, the persistence time is the lifetime of the transient, intermediate cell geometries during rearrangements (cf. Fig. 4). We found that persistence times are broadly distributed with a mean of 3.75 ± 1.90 min (CV = 0.51; $n = 41$ rearrangements in $N = 2$ embryos) [Fig. 5(c)]. These persistence times are longer than, but have a similar broad distribution as those reported for 2D analyses of vertex lifetimes at the apical side of the germband [42,52,53] and

2D vertex model simulations of tissues with active junction remodeling [54]. We did not find significant differences in persistence times between rearrangements initiated at different apical-basal positions [Supplemental Material Fig. S5B [37]].

Next, we analyzed the steps of lateral contact contraction and expansion over a time interval that included the first onset of contact contraction before neighbor exchange started and followed the growing contact after neighbor exchange concluded [Figs. 5(a), 5(d)–5(e′)]. In the first step of a typical rearrangement, the existing lateral contact narrows [Fig. 5(d); Supplemental Material Figs. S5C, S5C′ [37]]. Next, the new lateral contact forms and expands vertically along the apical-basal axis into a tall, narrow facet, while the existing lateral contact contracts and disappears [Fig. 5(d′), 5(e); Supplemental Material Figs. S5C, D [37]], similar to behavior observed in a recent study [26]. Finally, the new contact widens [Fig. 5(e′); Supplemental Material Fig. S5D′ [37]]. This sequence of events is supported by analyses of how lateral contact areas and heights change over time during cell rearrangements [Figs. 5(f), 5(g)]: the area of shrinking contacts typically begins decreasing prior to any decreases in contact height, and the height of growing contacts typically increases rapidly to full tissue height before area increases plateau, supporting the idea that changes in height and changes in width are distinct steps in lateral contact remodeling during rearrangement.

Finally, we quantified the rates of lateral contact area contraction and expansion. Focusing first on contracting contacts, we find that the majority of analyzed contacts initially contract slowly before transitioning to a fast contraction rate ($33 \pm 15\ \mu m^2/min$) (28/37 rearrangements in $N = 2$ embryos) [Figs. 5(h), 5(j); Supplemental Material Figs. S5E, E′, G; Supplemental Material Fig. S6 [37]]. In the other contacts, we find a similar contraction rate with no discernible initial slow phase [Supplemental Material Figs. S5E, E′, G; Supplemental Material Fig. S6 [37]]. For the expanding contacts, we find that the contacts expand at a fast rate ($42 \pm 23\ \mu m^2/min$) [Figs. 5(i), 5(j)], with a transient slow phase at the beginning (17/34 rearrangements in $N = 2$ embryos) or end (17/34 rearrangements) of the process [Fig. 5(i); Supplemental Material Fig. S5F, G; Supplemental Material Fig. S7 [37]]. We don't find significant differences in these rates between rearrangements initiated at different apical-basal positions [Supplemental Material Figs. S6E, F [37]].

Taken together, these findings illuminate the nature of lateral cell contact remodeling during epithelial cell rearrangements in 3D. We find that lateral contact remodeling proceeds via steps of lateral widening or narrowing and apical-basal shrinking or expansion. The broad distribution of persistence times is a signature of the rich cell dynamics below the apical tissue surface that gives rise to epithelial tissue remodeling during convergent extension.

III. DISCUSSION

We have shown that cell rearrangements in the *Drosophila* germband initiate at positions along the apical-basal axis of the tissue in a pattern that matches a gradient in cell packing structure along this axis. The apical-basal gradients in $\bar{p}^{2D}$ and Q that we find around the onset of GBE are reminiscent of the apical-basal patterns of myosin and E-cadherin localization in this tissue, and more generally of the polarized properties that are a defining feature of epithelia [5,8,9]. This is consistent with the idea that these structural gradients arise due to the appearance of planar polarized patterns of actomyosin near apical adherens junctions that induce anisotropic patterns of stress at this side of the tissue at the onset of GBE [8,9,41–43]. The attenuation of structural changes towards the basal side of the tissue highlights the challenge of coordinating mechanical behaviors at the apical and basal sides of this tall epithelium.

In 2D vertex models of epithelial tissues [55], preferred cell shapes and tissue structure are predictive of a tissue's propensity for cell rearrangements [15–18,21,56–58]. A critical value of $\bar{p}^{2D}$ distinguishes between rigid, solid-like and floppy, fluid-like behavior, with higher values of $\bar{p}^{2D}$ associated with more fluid-like behavior and lower barriers to cell rearrangement in isotropic tissues [15–18,21]. In anisotropic tissues like the germband, cell shape alignment Q can increase the critical $\bar{p}^{2D}$ for the rigidity transition [21]. Therefore, because we find that $\bar{p}^{2D}$ and Q *both* decrease together along the apical-basal axis, our results do not necessarily suggest a strong apical-basal gradient in tissue rigidity, at least within a 2D vertex model framework for predicting solid-fluid tissue behavior. A recent alternative 2D model of epithelial flow posits that the tissue behaves as an active solid that plastically flows due to evolving tension patterns at cell-cell contacts, which again can be inferred from cross-sectional cell shapes at the apical side of the tissue [51,59]. Future theoretical and modeling work that better capture the highly polarized and 3D nature of epithelial tissues will be essential for linking tissue structure to mechanics during 3D epithelial remodeling.

Although many cell rearrangements do initiate near the apical side of the tissue, our findings demonstrate that rearrangement initiation is not strictly localized to the apical domain, where contractile actomyosin is enriched [8–10], or to the basal domain, where protrusive activities have been reported [23]. Additionally, we show that during laterally initiated cell rearrangements, cell contact angles around the shrinking edge tend to change just prior to vertex formation in a manner that indicates an actively driven process in the lateral domain. These findings are consistent with the possibility that laterally initiated rearrangements are actively initiated by lateral actomyosin contractility, consistent with our observations of transient lateral myosin accumulation that precedes rearrangement initiation and propagation and with recent observations of lateral actomyosin activity during rearrangements [26], but do not rule out a role for passive rearrangement behaviors [60]. Future work will be required to uncover how rearrangement initiation is regulated by both molecular and mechanical cues, especially in basolateral regions that lack apparent strong planar polarity cues.

In addition, we have shown that cell rearrangements involve the apical-basal propagation of high-order vertices and lateral cell contact remodeling. Vertex propagation velocities vary as vertices traverse the apical-basal axis, indicating that differing mechanical and molecular environments may influence this process. Our pipeline for reconstructing and analyzing lateral cell-cell contacts allowed us to see how lateral contacts shrink and grow, with steps of lateral narrowing or

widening and apical-basal contraction or expansion. Future studies of protein dynamics in 3D will help to uncover how these lateral contact dynamics are regulated. Notably, we find that the cell rearrangement process involves transient cell geometries, such as scutoids, that are distinct from previously reported stable scutoids in curved tissues [27,29] or transient scutoids in proliferating tissues [32], revealing the complex cell dynamics below the apical tissue surface during convergent extension.

These findings raise the central question of what mechanisms regulate and coordinate cell rearrangement progression along the apical-basal tissue axis. Our results on myosin localization patterns and cell contact angles, together with recent reports in the literature [26], point to a role for local, myosin-dependent active forces distributed along lateral contacts, suggesting that rearrangement progression might be actively regulated and driven. This raises the question of the molecular and mechanical mechanisms regulating myosin localization and activity on lateral cell contacts as well as the propagation of that activity during rearrangement progression. Notably, we do see a subset of cell rearrangements that lack detectable lateral myosin and do not show contact angle patterns indicative of local active tensions, suggesting that some rearrangements may instead be the result of active stresses exerted at the apical surface and that propagation represents passive relaxation of those apical stresses. Our findings linking cell rearrangement initiation and high-order vertex propagation to tissue structure suggest that local tissue structural and/or mechanical properties may influence the patterns of rearrangement along the apical-basal axis of the tissue. Future studies of genetic mutants will be needed to uncover the molecular and mechanical mechanisms that coordinate rearrangement progression across the epithelium to produce efficient tissue remodeling. The findings and approaches reported here will be a foundation for tackling this question. More broadly, the principles of 3D cell rearrangements we have uncovered and the approaches for quantifying 3D epithelial tissue structure we have developed should be broadly applicable to other epithelia that remodel during development or in disease.

IV. MATERIALS AND METHODS

A. Fly stocks and genetics

Embryos were generated at 23 °C and analyzed at room temperature. Embryos were progeny of *yw* females with two copies of a sqh-gap43:mCherry transgene to label cell membranes [61] or of *yw* females with two copies of a sqh-gap43:mCherry transgene and two copies of a sqh-GFP:ZipWT transgene to label cell membranes and non-muscle myosin II heavy chain [62], respectively.

B. Embryo preparation

1. Live imaging

Embryos aged 2–4 hr were dechorionated for 2 min in 50% (vol/vol) bleach, washed in distilled water, and mounted in a 1:1 mixture of halocarbon oils 27 and 700 between a coverslip and an oxygen-permeable membrane (YSI).

2. Fixation and immunofluorescence

Embryos aged 3-6 hr were dechorionated for 2 min in 50% (vol/vol) bleach, washed in distilled water, and fixed in 3.7% (vol/vol) formaldehyde (Sigma Aldrich) in 0.1 M sodium phosphate (pH 7.4) and heptane for 1 hr. After fixation, embryos were manually devitellinized. The primary antibody rabbit anti-GFP (Torrey Pines Biolabs) was used at 1:100, and the primary antibody rat anti-DE-cadherin DCAD2 (Developmental Studies Hybridoma Bank) was used at 1:25. A goat anti-rabbit secondary antibody conjugated to Alexa-488 (Invitrogen) and goat anti-rat secondary antibody conjugated to Alexa-633 (Invitrogen) were both used at 1:500. An Alexa-568 conjugated phalloidin (Invitrogen) was used at 1:100. Embryos were mounted using ProLong Gold antifade reagent (Invitrogen).

C. Confocal imaging

1. Live imaging

Embryos were oriented with the cephalic and ventral furrow visible at the edges of the field of view. A 212 μm × 159 μm ventrolateral region of the embryo was imaged on a Zeiss LSM880 laser-scanning confocal microscope using the 561 nm laser line, 40×/1.2 NA water-immersion objective, and the Zeiss AiryScan detector. *Z* stacks were acquired at 1 μm steps and 13–15 sec intervals with in-plane resolution of 0.33 μm × 0.33 μm. Mean intensity *z* projections of three consecutive slices were analyzed at each *z* position along the apical-basal axis.

For embryos with both the sqh-gap43:mCherry and sqh-GFP:ZipWT transgenes, *z* stacks were acquired at 2 μm steps and 13–15 sec intervals with in-plane resolution of 0.13 μm × 0.13 μm. Mean intensity *z* projections of three consecutive slices were analyzed at each *z* position along the apical-basal axis for the membrane channel and max intensity *z* projections of three consecutive slices were analyzed at each *z* position along the apical-basal axis for the myosin channel.

2. Imaging of fixed embryos

Stage 6 and 7 embryos that were oriented with ventral or dorsal sides towards the cover slip were selected for imaging. A focal plane at the middle of the embryo was selected to capture a sagittal view of the germband. A 100 μm × 100 μm region was imaged on a Zeiss LSM880 laser-scanning confocal microscope using the 488, 561, and/or 633 nm laser lines, 40X/1.2 NA water-immersion objective, Zeiss AiryScan detector, and 0.1 μm pixel size. Laser power and scan speed were chosen to maximize the dynamic range for each channel without saturating high-intensity regions and to minimize photobleaching.

D. Image analysis

1. Apical z-position determination and z-drift correction

A kymograph was performed on a line parallel to the apical-basal axis that bisected the midsagittal view of the embryo to determine the location of the most apical *z* plane of the tissue at all time points. If the location of the most apical *z* plane varied over time, manual registration of *z* planes

was performed. The most apical z plane was defined as $z = 0$ for comparisons across multiple time points and multiple embryos.

2. Measurement of tissue elongation along the anterior-posterior axis

Tissue elongation was measured by particle image velocimetry (PIV) using **openPIV** in **Python**. Each image was divided into two-pass fast Fourier transform windows (50×50 pixels) with 30% overlaps. A displacement vector field for each window and each time point was determined by cross-correlating each window in the current time point and the image in the next time point.

Tissue length change was measured by quantifying the cumulative sum of the anterior-directed displacement at the anterior end of the germband and the posterior-directed displacement at the posterior end of the germband. The onset of tissue elongation ($T = 0$) was defined as the time point when the derivative of the tissue elongation curve intersects zero at the most apical side of the tissue. Embryos were registered in time using the onset of tissue elongation for multiple embryo comparisons.

3. Cell segmentation and tracking

We segmented 3D movies of gap43:mCherry one z plane at a time, restricting analysis to z planes with sufficient image quality for segmentation (typically $z = 2$–$21\,\mu$m). First, we generated automated cell segmentations for each z plane using a fine-tuned instance of the **cyto2** model in **CellPose 2.0** [63]. Next, we processed each z plane using morphological operations in **scikit-image** [64] to remove holes, isolated connected components, and any spaces between cell masks until a confluence criterion was met. The cell masks from the automated cell segmentations were converted from pixel-based representations to straight-edged polygonal outlines.

We then stitched 2D masks into 3D volumes using the **stitch3D** function in **CellPose** and tracked cells over time using **btrack** [65]. Cells with fewer than three sides or with unequal number of sides and vertices were considered segmentation errors and eliminated from the set of cells used for analysis.

Automated cell segmentations were validated against cell outlines manually corrected in the **MATLAB** package **SEGGA** [43]. Predefined regions of interest in the most apical and basolateral z planes and subsequent z planes in between at intervals of 2–5 μm were manually corrected and compared to the same selected regions in the automated segmentations. The validated automated cell segmentation data formed the basis for the analysis of cell and tissue morphology and for the 3D reconstruction of lateral cell-cell contacts. For the analysis of rearrangement events per cell, we used the manually corrected segmentations in **SEGGA**, as it includes built-in functionality for this analysis.

4. Identification and tracking of cell rearrangements

For the analysis reported in Figs. 2 and 3, we identified a subset of all cell rearrangements in each movie by visual inspection and manual tracking of the positions of the associated high-order vertices over time and over the apical-basal axis. Cell rearrangements used for analysis were identified by searching for high-order vertices that formed from a shrinking edge and resolved into a new edge at all z positions within the ROI during the movie. Classification of the identified cell rearrangement was based on the initiation location falling within the set ranges along the apical-basal axis [Fig. 2(d)]. If consecutive z positions initiated at the same time, the median z position was used as the initiation location.

High-order vertex formation and resolution into edges were tracked for identified cell rearrangements. Only cell rearrangements involving four cells (T1 processes) were included in analyses for Fig. 2, and cell rearrangements involving four or more cells were included in analyses for Fig. 3. For the lateral contact height analyses reported in Figs. 5(f) and 5(g), height is the z span of the lateral contact and was manually measured based on the apical-basal location of high-order vertices during each cell rearrangement. For Fig. 5(f), contact area and height were smoothed using a rolling average calculated over five consecutive time frames.

5. High-order vertex velocity analysis

For unidirectional rearrangements (apical and basolateral), velocity was calculated by dividing the distance traversed (18 μm) by the difference in time between high-order vertex formation at the apical most z position and basal most z position. For multidirectional rearrangements (lateral and multifocal), two velocities were calculated by dividing the distance between initiation (lateral) or termination (multifocal) position and apical or basal most z position by the difference in time between high-order vertex formation at initiation or termination position and apical or basal most z position. High-order vertex propagation velocity for multidirectional rearrangements was divided into apical or basal direction of propagation.

Velocity data for each rearrangement type were combined from three embryos for statistical analysis as the difference between the average propagation velocities in the three embryos was not statistically significant [Supplemental Material Fig. S3 [37]]. Velocity data for basolateral and multifocal rearrangements were automatically combined from three embryos due to small sample size.

6. Velocity breakpoint analysis

We used piecewise (segmented) linear regression [66] of vertex propagation along the apical-basal axis to estimate potential changes in vertex propagation velocity. We allowed the preset number of breakpoints to vary between 0 and 3 and visually inspected each fit to select the best fits. We used the **Python** package **piecewise-regression** [67].

7. Myosin localization during cell rearrangements

For the analyses reported in Fig. 3, we identified the presence and location of myosin accumulation during cell rearrangements by visual inspection and manual tracking using the Fiji distribution of ImageJ [68,69].

8. Analysis of protein localization patterns in fixed samples

Intensity measurements along the apical-basal axis for myosin, E-cadherin, and F-actin reported in Fig. 3 were acquired from three fixed embryos at developmental stages 6 and 7. Imaging was performed on lateral views of the germband and analyzed using the Fiji distribution of ImageJ [68,69]. For each embryo, five rectangular sample regions, approximately 2 μm wide, 25 μm tall, and spanning the apical-basal height of lateral cell contacts within the tissue, were selected. Intensity was averaged along the horizontal axis within each region, and the resulting apical-basal profiles were then averaged across the five regions for each embryo.

E. 2D tissue network reconstruction

Analysis of the cell outline network topology and 3D reconstructions required us to convert the cell segmentations into planar tilings with explicitly defined nodes and edges that formed each polygonal cell. We extracted the cell outline network in each z plane from cell outline skeleton masks and converted the skeleton mask into a graph where multicellular junctions formed the nodes and bicellular junctions formed the edges, and each cell was represented as a polygon. These data formed the basis for the calculation of the vertex coordination number $\mathcal{Z}$, the cell shape index p^{2D}, the triangle elongation tensor $\boldsymbol{q}$, the cell shape alignment index Q, and the cell rearrangement rates.

F. 3D cell and tissue reconstruction

We used a custom 3D reconstruction pipeline to infer 3D cell geometry from segmented z stacks of the cell outline marker. To ensure a confluent tissue and spatially consistent reconstructions, we used a constrained 3D cell surface triangulation procedure as follows: (i) a cell outline skeleton mask was extracted from the cell segmentations in each z plane; (ii) the skeleton mask was converted into a graph by identifying and labeling the nodes and edges of the cell outline network; (iii) the set of nodes and edges that defined each lateral cell-cell contact were identified and isolated across the entire z stack; (iv) lateral cell-cell contact surfaces were triangulated while using the constituent nodes and edges as spatial constraints; and (v) finally, each cell was reassembled as a set of lateral, apical, and basal triangulated surface patches.

This approach avoids the common pitfalls of conventional surface triangulation recipes like the marching cubes algorithm and preserves the curvature distributions of lateral cell-cell contact surfaces when applied to data with anisotropic voxel resolutions. It also provides direct access to the morphology and deformations of each individual cell-cell contact. This approach is similar to the one implemented in [70]. We built the pipeline in Python using `scikit-image` [64], `sknw` [71], and `pyvista` [72]. We used ParaView [73] to create the 3D renderings in Figs. 4 and 5.

G. Quantification of cell and tissue structure

1. Vertex coordination number

Each vertex of the cell contact network has an associated coordination number $\mathcal{Z}$, equal to the number of edges it connects. The ROI-averaged vertex coordination number $\bar{\mathcal{Z}}$ is the average number of cells meeting at a single vertex. A threshold edge length of 0.75 μm was determined manually and led to results consistent with prior reports [21].

2. Cell rearrangement rate

We measured the cell rearrangement rate in each z plane by tracking the number of neighbors lost per cell per unit time in the ROI using `SEGGA` as described in [43].

3. Cell shape index

The 2D cell shape index is defined as the ratio of the cell perimeter to the square root of cell area, $p^{2D} = P/\sqrt{A}$ (Fig. 1). The tissue average cell shape index, $\bar{p}^{2D}$, is the mean of p^{2D} over all cells in a given region of interest. We computed the cell shape index using polygonal approximations of the cell mask outlines (unless stated otherwise).

4. Cell shape alignment index

The cell shape alignment index was computed using a triangulation of the cell outline network as described in [38] and demonstrated in [21]. Briefly, the tissue plane is tiled with triangles that are formed by connecting the cell barycenters and high-order vertices (those with $\mathcal{Z} > 3$) (Fig. 1). In the resulting tiling, the elongation, $\boldsymbol{q}$, of each triangle with respect to an equilateral reference triangle provides a measure of local cell shape anisotropy and the area-weighted average $\boldsymbol{Q} = \langle \boldsymbol{q} \rangle$ provides an aggregate measure of shape anisotropy of the cell network. The magnitude of this tensor, $Q = (Q_{xx}^2 + Q_{xy}^2)^{1/2}$, called the *cell shape alignment index*, provides a scalar measure of tissue anisotropy. The triangle elongation tensor, $\boldsymbol{q}$, and the cell shape alignment index, Q, were both calculated using the Python package `triangles-segga` [21].

5. Cell contact angles during cell rearrangements

For results in Figs. 3(f)–3(h), an automated method was used to determine cell contact angles. Briefly, a vertex and its connected edges, based on the skeleton masks of cells involved in the rearrangement, were used to determine the contact angle and to account for cell edge curvature. On each edge, edge points 5 pixels away from the selected node were used to calculate the cell angle. For results in Fig. 3(j), a manual method was used. Briefly, the average contact angle was determined manually from five consecutive time frames using the Fiji distribution of ImageJ.

6. Analysis of lateral contact remodeling during rearrangements

We analyzed the geometry and kinetics of lateral cell-cell contact remodeling by 3D reconstruction of contact surfaces to measure the change in contact surface areas over time. Each pairwise contact surface was triangulated as described previously, and we calculated the surface area by summing up the areas of the constituent triangles.

7. Rearrangement time

We estimated a *rearrangement time* defined as the cross-over point of the contracting and expanding contact area time series [Fig. 5(a)]. We first identified the contracting and

expanding contact surfaces in each group of four cells involved in a rearrangement. We then found the point where the two curves intersected after smoothing both curves using a boxcar moving average filter with size equal to 20 timepoints for the calculations reported in Fig. 5.

8. Persistence time

We defined the *persistence time* as the interval defined by (1) the growing edge increasing beyond a minimum threshold surface area on one hand and (2) the contracting edge surface area decreasing below the same minimum threshold on the other. We used a minimum threshold surface area of 10 μm^2 in the calculations reported in Fig. 5 and Supplemental Material Figs. S5–S7 [37].

9. Contact remodeling rates

We used piece-wise (segmented) linear regression [66] of the contact area time series to estimate the rates of contact contraction and expansion during rearrangements and potential rate changes in each curve. We allowed the preset number of breakpoints to vary between 1 and 3 and visually inspected each fit to select the best fits. We used the `Python` package `piecewise-regression` [67]. We used the Mann-Whitney U test to compare the rates of contact contraction and expansion for the results reported in Fig. 5 and Supplemental Material Figs. S5–S7 [37].

ACKNOWLEDGMENTS

We thank Ann Sutherland, Shiladitya Banerjee, Xinzhi Li, and members of the Kasza Lab for helpful discussions and comments on the manuscript. This work was supported by NIH Grant No. R35GM138380 to K.E.K.; K.E.K. is the recipient of an NSF CAREER Award, Packard Fellowship, and Sloan Research Fellowship in Physics.

X.W. and K.E.K. conceived the initial studies of tissue structure variation along the apical-basal axis. X.W. performed proof-of-concept experiments and initial analyses of tissue structure. E.M.K. and K.E.K. conceived the manual analyses of vertex dynamics and cell rearrangements along the apical-basal axis. S.O. and K.E.K. conceived the analyses of lateral cell-cell contact remodeling. E.M.K. generated the fly stocks and performed the imaging experiments. S.O. and E.M.K. developed the image analysis pipeline. E.M.K. performed manual analyses of high-order vertex initiation and propagation. S.O. and X.L. designed the 3D reconstruction pipeline. X.L. implemented and tested the 3D reconstruction pipeline. E.M.K., S.O., X.L., and T.L. performed the quantitative analyses of cell-level and tissue-level imaging data. S.O., E.M.K., and K.E.K. wrote the first manuscript draft, and all authors contributed to the final manuscript.

DATA AVAILABILITY

The data that support the findings of this article are not publicly available upon publication because it is not technically feasible and/or the cost of preparing, depositing, and hosting the data would be prohibitive within the terms of this research project. The data are available from the authors upon reasonable request. The pipeline for 3D reconstruction of lateral cell-cell contacts is available from the authors upon reasonable request.

[1] C.-P. Heisenberg and Y. Bellaıche, Forces in tissue morphogenesis and patterning, Cell **153**, 948 (2013).
[2] B. Ladoux and R.-M. Mège, Mechanobiology of collective cell behaviours, Nat. Rev. Mol. Cell Biol. **18**, 743 (2017).
[3] E. Walck-Shannon and J. Hardin, Cell intercalation from top to bottom, Nat. Rev. Mol. Cell Biol. **15**, 34 (2014).
[4] S. B. Lemke and C. M. Nelson, Dynamic changes in epithelial cell packing during tissue morphogenesis, Curr. Biol. **31**, R1098 (2021).
[5] A. C. Paré and J. A. Zallen, Cellular, molecular, and biophysical control of epithelial cell intercalation, Curr. Top. Dev. Biol. **136**, 167 (2020).
[6] R. M. Herrera-Perez and K. E. Kasza, Biophysical control of the cell rearrangements and cell shape changes that build epithelial tissues, Curr. Opin. Genet. Dev. **51**, 88 (2018).
[7] K. D. Irvine and E. Wieschaus, Cell intercalation during *Drosophila* germband extension and its regulation by pair-rule segmentation genes, Development **120**, 827 (1994).
[8] J. A. Zallen and E. Wieschaus, Patterned gene expression directs bipolar planar polarity in *Drosophila*, Dev. Cell **6**, 343 (2004).
[9] C. Bertet, L. Sulak, and T. Lecuit, Myosin-dependent junction remodelling controls planar cell intercalation and axis elongation, Nature (London) **429**, 667 (2004).
[10] J. T. Blankenship, S. T. Backovic, J. S. P. Sanny, O. Weitz, and J. A. Zallen, Multicellular rosette formation links planar cell polarity to tissue morphogenesis, Dev. Cell **11**, 459 (2006).
[11] R. Fernandez-Gonzalez, S. de Matos Simoes, J.-C. Röper, S. Eaton, and J. A. Zallen, Myosin II dynamics are regulated by tension in intercalating cells, Dev. Cell **17**, 736 (2009).
[12] M. Rauzi, P.-F. Lenne, and T. Lecuit, Planar polarized actomyosin contractile flows control epithelial junction remodelling, Nature (London) **468**, 1110 (2010).
[13] A. Paré, A. Vichas, C. Fincher, Z. Mirman, D. Farrell, A. Mainieri, and J. Zallen, A positional toll receptor code directs convergent extension in *Drosophila*, Nature (London) **515**, 523 (2014).
[14] R. Farhadifar, J.-C. Röper, B. Aigouy, S. Eaton, and F. Jülicher, The influence of cell mechanics, cell-cell interactions, and proliferation on epithelial packing, Curr. Biol. **17**, 2095 (2007).
[15] D. Bi, J. H. Lopez, J. M. Schwarz, and M. L. Manning, A density-independent rigidity transition in biological tissues, Nat. Phys. **11**, 1074 (2015).
[16] D. Bi, X. Yang, M. C. Marchetti, and M. L. Manning, Motility-driven glass and jamming transitions in biological tissues, Phys. Rev. X **6**, 021011 (2016).
[17] J.-A. Park, J. H. Kim, D. Bi, J. A. Mitchel, N. T. Qazvini, K. Tantisira, C. Y. Park, M. McGill, S.-H. Kim, B. Gweon *et al.*,

Unjamming and cell shape in the asthmatic airway epithelium, Nat. Mater. **14**, 1040 (2015).

[18] X. Yang, D. Bi, M. Czajkowski, M. Merkel, M. L. Manning, and M. C. Marchetti, Correlating cell shape and cellular stress in motile confluent tissues, Proc. Natl. Acad. Sci. USA **114**, 12663 (2017).

[19] L. Atia, D. Bi, Y. Sharma, J. A. Mitchel, B. Gweon, S. A. Koehler, S. J. DeCamp, B. Lan, J. H. Kim, R. Hirsch, A. F. Pegoraro *et al.*, Geometric constraints during epithelial jamming, Nat. Phys. **14**, 613 (2018).

[20] R. Tetley, M. Staddon, D. Heller, A. Hoppe, S. Banerjee, and Y. Mao, Tissue fluidity promotes epithelial wound healing, Nat. Phys. **15**, 1195 (2019).

[21] X. Wang, M. Merkel, L. B. Sutter, G. Erdemci-Tandogan, M. L. Manning, and K. E. Kasza, Anisotropy links cell shapes to tissue flow during convergent extension, Proc. Natl. Acad. Sci. USA **117**, 13541 (2020).

[22] M. Williams, W. Yen, X. Lu, and A. Sutherland, Distinct apical and basolateral mechanisms drive planar cell polarity-dependent convergent extension of the mouse neural plate, Dev. Cell **29**, 34 (2014).

[23] Z. Sun, C. Amourda, M. Shagirov, Y. Hara, T. E. Saunders, and Y. Toyama, Basolateral protrusion and apical contraction cooperatively drive *Drosophila* germ-band extension, Nat. Cell Biol. **19**, 375 (2017).

[24] S. Weng, R. J. Huebner, and J. B. Wallingford, Convergent extension requires adhesion-dependent biomechanical integration of cell crawling and junction contraction, Cell Rep. **39**, 110666 (2022).

[25] A. Saraswathibhatla and J. Notbohm, Tractions and stress fibers control cell shape and rearrangements in collective cell migration, Phys. Rev. X **10**, 011016 (2020).

[26] T. Vanderleest, X. Yi, R. Budhathoki, K. Linvill, C. Hobson, J. Heddleston, D. Loerke, and T. Blankenship, Lattice light sheet microscopy reveals 4D force propagation dynamics and leading-edge behaviors in an embryonic epithelium in *Drosophila*, Curr. Biol. **34**, 3165 (2024).

[27] P. Gómez-Gálvez, P. Vicente-Munuera, A. Tagua, C. Forja, A. M. Castro, M. Letrán, A. Valencia-Expósito, C. Grima, M. Bermúdez-Gallardo, Ó. Serrano-Pérez-Higueras *et al.*, Scutoids are a geometrical solution to three-dimensional packing of epithelia, Nat. Commun. **9**, 2960 (2018).

[28] H. F. Gomez, M. S. Dumond, L. Hodel, R. Vetter, and D. Iber, 3D cell dynamics in growing pseudostratified epithelia, eLife **10**, e68135 (2021).

[29] J.-F. Rupprecht, K. H. Ong, J. Yin, A. Huang, H.-H.-Q. Dinh, A. P. Singh, S. Zhang, W. Yu, and T. E. Saunders, Geometric constraints alter cell arrangements within curved epithelial tissues, Mol. Biol. Cell **28**, 3582 (2017).

[30] D. Iber and R. Vetter, 3D organisation of cells in pseudostratified epithelia, Front. Phys. **10**, 898160 (2022).

[31] Y. Lou, J.-F. Rupprecht, S. Theis, T. Hiraiwa, and T. E. Saunders, Curvature-induced cell rearrangements in biological tissues, Phys. Rev. Lett. **130**, 108401 (2023).

[32] V. Barone, A. Tagua, J. Á. A.-S. Román, A. Hamdoun, J. Garrido-García, D. C. Lyons, and L. M. Escudero, Local and global changes in cell density induce reorganisation of 3D packing in a proliferating epithelium, Development **151**, dev202362 (2024).

[33] A. Mughal, S. J. Cox, D. Weaire, S. R. Burke, and S. Hutzler, Demonstration and interpretation of 'scutoid' cells formed in a quasi-2D soap froth, Philos. Mag. Lett. **98**, 358 (2018).

[34] R. M. Herrera-Perez, C. Cupo, C. Allan, A. B. Dagle, and K. E. Kasza, Tissue flows are tuned by actomyosin-dependent mechanics in developing embryos, PRX Life **1**, 013004 (2023).

[35] X. Wang, C. M. Cupo, S. Ostvar, A. D. Countryman, and K. E. Kasza, E-cadherin tunes tissue mechanical behavior before and during morphogenetic tissue flows, Curr. Biol. **34**, 3367 (2024).

[36] D. Bi, J. H. Lopez, J. M. Schwarz, and M. L. Manning, Energy barriers and cell migration in densely packed tissues, Soft Matter **10**, 1885 (2014).

[37] See Supplemental Material at http://link.aps.org/supplemental/10.1103/l5r5-pb9t for seven additional supplemental figures and captions.

[38] M. Merkel, R. Etournay, M. Popović, G. Salbreux, S. Eaton, and F. Jülicher, Triangles bridge the scales: Quantifying cellular contributions to tissue deformation, Phys. Rev. E **95**, 032401 (2017).

[39] M. Rauzi, U. Krzic, T. E. Saunders, M. Krajnc, P. Ziherl, L. Hufnagel, and M. Leptin, Embryo-scale tissue mechanics during *Drosophila* gastrulation movements, Nat. Commun. **6**, 8677 (2015).

[40] C. Cupo, C. Allan, V. Ailiani, and K. E. Kasza, Signatures of structural disorder in the developing *Drosophila* germband epithelium, PRX Life **2**, 043004 (2024).

[41] M. Rauzi, P. Verant, T. Lecuit, and P.-F. Lenne, Nature and anisotropy of cortical forces orienting *Drosophila* tissue morphogenesis, Nat. Cell Biol. **10**, 1401 (2008).

[42] K. E. Kasza, D. L. Farrell, and J. A. Zallen, Spatiotemporal control of epithelial remodeling by regulated myosin phosphorylation, Proc. Natl. Acad. Sci. USA **111**, 11732 (2014).

[43] D. L. Farrell, O. Weitz, M. O. Magnasco, and J. A. Zallen, Segga: A toolset for rapid automated analysis of epithelial cell polarity and dynamics, Development **144**, 1725 (2017).

[44] A. John and M. Rauzi, A two-tier junctional mechanism drives simultaneous tissue folding and extension, Dev. Cell **56**, 1469 (2021).

[45] T. Lecuit and E. Wieschaus, Polarized insertion of new membrane from a cytoplasmic reservoir during cleavage of the *Drosophila* embryo, J. Cell Biol. **150**, 849 (2000).

[46] L. Figard, H. Xu, H. G. Garcia, I. Golding, and A. M. Sokac, The plasma membrane flattens out to fuel cell surface growth during *Drosophila* cellularization, Dev. Cell **27**, 648 (2013).

[47] K. K. Chiou, L. Hufnagel, and B. I. Shraiman, Mechanical stress inference for two dimensional cell arrays, PLoS Comput. Biol. **8**, e1002512 (2012).

[48] S. Ishihara and K. Sugimura, Bayesian inference of force dynamics during morphogenesis, J. Theor. Biol. **313**, 201 (2012).

[49] W. Kong, O. Loison, P. C. Shivakumar, E. H. Chan, M. Saadaoui, C. Collinet, P.-F. Lenne, and R. Clément, Experimental validation of force inference in epithelia from cell to tissue scale, Sci. Rep. **9**, 14647 (2019).

[50] N. Noll, S. J. Streichan, and B. I. Shraiman, Variational method for image-based inference of internal stress in epithelial tissues, Phys. Rev. X **10**, 011072 (2020).

[51] F. Brauns, N. H. Claussen, E. F. Wieschaus, and B. I. Shraiman, The geometric basis of epithelial convergent extension, eLife **13**, RP95521 (2024).

[52] M. Tamada, D. L. Farrell, and J. A. Zallen, Abl regulates planar polarized junctional dynamics through β-catenin tyrosine phosphorylation, Dev. Cell **22**, 309 (2012).
[53] C. Collinet, M. Rauzi, P.-F. Lenne, and T. Lecuit, Local and tissue-scale forces drive oriented junction growth during tissue extension, Nat. Cell Biol. **17**, 1247 (2015).
[54] F. Pérez-Verdugo and S. Banerjee, Tension remodeling regulates topological transitions in epithelial tissues, PRX Life **1**, 023006 (2023).
[55] A. G. Fletcher, M. Osterfield, R. E. Baker, and S. Y. Shvartsman, Vertex models of epithelial morphogenesis, Biophys. J. **106**, 2291 (2014).
[56] E. Lawson-Keister and M. L. Manning, Jamming and arrest of cell motion in biological tissues, Curr. Opin. Cell Biol. **72**, 146 (2021).
[57] P.-F. Lenne and V. Trivedi, Sculpting tissues by phase transitions, Nat. Commun. **13**, 664 (2022).
[58] E. Hannezo and C.-P. Heisenberg, Rigidity transitions in development and disease, Trends Cell Biol. **32**, 433 (2022).
[59] N. Claussen, F. Brauns, and B. Shraiman, A geometric-tension-dynamics model of epithelial convergent extension, Proc. Natl. Acad. Sci. USA **121**, e2321928121 (2024).
[60] R. Tetley and Y. Mao, The same but different: Cell intercalation as a driver of tissue deformation and fluidity, Philos. Trans. R. Soc. B **373**, 20170328 (2018).
[61] A. Martin, M. Gelbart, R. Fernandez-Gonzalez, M. Kaschube, and E. Wieschaus, Integration of contractile forces during tissue invagination, J. Cell Biol. **188**, 735 (2010).
[62] K. E. Kasza, S. Supriyatno, and J. A. Zallen, Cellular defects resulting from disease-related myosin II mutations in *Drosophila*, Proc. Natl. Acad. Sci. USA **116**, 22205 (2019).
[63] M. Pachitariu and C. Stringer, Cellpose 2.0: How to train your own model, Nat. Methods **19**, 1634 (2022).
[64] S. Van der Walt, J. L. Schönberger, J. Nunez-Iglesias, F. Boulogne, J. D. Warner, N. Yager, E. Gouillart, and T. Yu, Scikit-image: Image processing in Python, PeerJ **2**, e453 (2014).
[65] K. Ulicna, G. Vallardi, G. Charras, and A. R. Lowe, Automated deep lineage tree analysis using a Bayesian single cell tracking approach, Front. Comput. Sci. **3**, 734559 (2021).
[66] V. M. R. Muggeo, Estimating regression models with unknown break-points, Stat. Med. **22**, 3055 (2003).
[67] C. Pilgrim, Piecewise-regression (aka segmented regression) in Python, J. Open Source Softw. **6**, 3859 (2021).
[68] J. Schindelin, I. Arganda-Carreras, E. Frise, V. Kaynig, M. Longair, T. Pietzsh, S. Preibisch, C. Rueden, S. Saalfeld, B. Schmid *et al.*, Fiji: An open-source platform for biological-image analysis, Nat. Methods **9**, 676 (2012).
[69] C. Rueden, J. Schindelin, M. Hiner, B. DeZonia, A. Walter, E. Arena, and K. Eliceiri, ImageJ2: ImageJ for the next generation of scientific image data, BMC Bioinf. **18**, 529 (2017).
[70] M. A. Gelbart, B. He, A. C. Martin, S. Y. Thiberge, E. F. Wieschaus, and M. Kaschube, Volume conservation principle involved in cell lengthening and nucleus movement during tissue morphogenesis, Proc. Natl. Acad. Sci. USA **109**, 19298 (2012).
[71] X. Yan and C. Christensen, sknw: Skeleton analysis in Python, Version 0.15 (Python Package Index, 2017).
[72] C. Sullivan and A. Kaszynski, PyVista: 3D plotting and mesh analysis through a streamlined interface for the Visualization Toolkit (VTK), J. Open Source Softw. **4**, 1450 (2019).
[73] U. Ayachit, *The Paraview Guide: A Parallel Visualization Application* (Kitware, Clifton Park, NY, 2015).